

# Ultra Strong Magnon-Photon Coupling Achieved by Magnetic Films in Contact with Superconducting Resonators

Alberto Ghirri\*

*Istituto Nanoscienze - CNR, Centro S3, via G. Campi 213/A, 41125, Modena, Italy*

Claudio Bonizzoni and Marco Affronte

*Dipartimento di Scienze Fisiche, Informatiche e Matematiche Università di Modena e Reggio Emilia,*

*via G. Campi 213/A, 41125, Modena, Italy and*

*Istituto Nanoscienze - CNR, Centro S3, via G. Campi 213/A, 41125, Modena, Italy*

Maksut Maksutoglu

*Physics Department, Gebze Technical University, 41400, Gebze, Kocaeli, Turkey*

Alberto Mercurio, Omar Di Stefano, and Salvatore Savasta

*Dipartimento di Scienze Matematiche e Informatiche,*

*Scienze Fisiche e Scienze della Terra, Università di Messina, I-98166 Messina, Italy*

(Dated: February 3, 2023)

Coherent coupling of magnon excitations and microwave photons in a cavity may disclose new paths to unconventional phenomena and for novel applications. Here, we show that large couplings and cooperativities can be achieved with YIG (Yttrium Iron Garnet) films in contact with coplanar resonators made of superconducting YBCO. Transmission spectra, which are analysed by a modified Hopfield model, show that the coupling of the dominant magnetic mode with photons exceeds 0.2 times the cavity frequency, thus demonstrating the achievement of the ultra strong coupling regime with this architecture.

The interplay between magnetic excitations and electromagnetic radiation has recently assumed a pivotal role in many fields of research such as magnonics, spintronics, magneto-opto-mechanics and information processing for its potentialities in the development of hybrid systems and devices [1–3]. The prototypical case is that of a magnetically ordered sample in a cavity field, where the coupling takes place between magnetic excitations and the resonant monochromatic electromagnetic mode [4]. The former, already studied in a series of seminal experimental [5] and theoretical [6] works, are usually modelled by the Landau-Lifshitz-Gilbert (LLG) equation [7]. This description works remarkably well in the case of the ferrimagnetic Yttrium Iron Garnet (YIG) for which the dispersion law of magnetic excitations have been studied in detail in different cases and geometries [8] and for which key parameters are well documented in literature [9]. YIG is also largely used in key experiments and many applications thanks to combination of several optimal features, including one of the lowest Gilbert (damping) coefficient  $\alpha \approx 10^{-5}$  reported for magnetic materials [2]. A more fundamental issue is the description of the magnetic-cavity system in the quantum regime. In the first instance, one can refer to the Dicke model considering the spin waves as collective (bosonic) excitations (magnons) interacting with photons in a cavity. Models for treating such a general problem have been developed to describe a large variety of hybrid light-matter systems including cold atoms or solid state qubits.

There is a general trend now to push these stud-



FIG. 1. (a) Schematic representation of the YBCO/sapphire CPW resonator with the YIG/GGG film positioned on top. (b) Finite-element simulation of the distribution of the magnetic field  $\mathbf{h}_{\text{ac}}$  for the fundamental mode of the resonator. Dashed lines delimit the width of the GGG substrate.

ies beyond the conventional coupling regimes and more specifically to reach coupling strengths  $\lambda$  being a non negligible fraction of the cavity frequency  $\omega_c$  [10, 11]. For  $\lambda/\omega_c \geq 0.1$  we refer to the ultra strong coupling regime (USC), in which unconventional effects are expected due to the strong correlation between spins and photons. Classical input-output formalism and Jaynes (Tavis)-Cummings model have been mainly used so far to interpret data. Yet, an appropriate modelling of magnetic excitations coupled ultra strongly with microwave photons in the cavity is still lacking. In particular, the description of the fundamental interaction between the electromagnetic field and the magnetic system, including the diamagnetic term, which plays a key role for the superradiant phase transition [12–15], still need to be clarified and tested on real magnetic materials. There are few

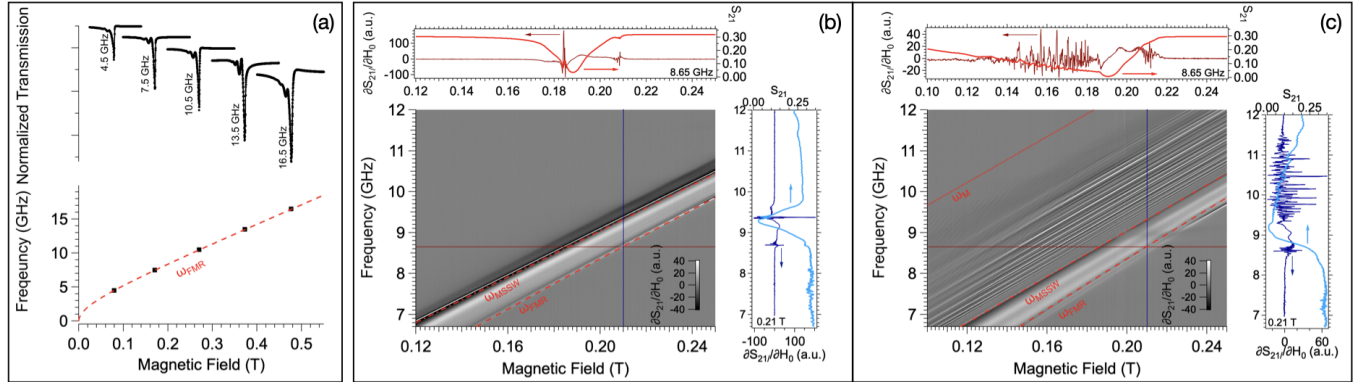


FIG. 2. Characterization of the YIG film by broadband transmission spectroscopy. The incident microwave power is  $P_{inc} = -8$  dBm. (a) Ag/alumina microstrip, case #A. Top: field-swept transmission spectra (temperature  $T = 50$  K), taken at different continuous wave frequencies, as indicated. Bottom: plot of the excitation frequencies as a function of the measured resonance field; the dashed line shows the fit with Eq. 1. (b) YBCO/sapphire CPW line, case #B ( $T = 30$  K). Center: Spectral map showing  $\partial S_{21}(\omega, H_0)/\partial H_0$ . Top: Plot of  $S_{21}$  and  $\partial S_{21}/\partial H_0$  as function of  $H_0$  for  $\omega/2\pi = 8.65$  GHz. Right: Plot of  $S_{21}$  and  $\partial S_{21}/\partial H_0$  as function of  $\omega$  for  $H_0 = 0.21$  T. (c) Same as (b) with YIG in contact with the CPW line, case #C.

experimental reports for magnetic systems achieving (ultra) strong coupling regime with resonant cavities. The case of a sphere of the prototypical ferrimagnetic Yttrium Iron Garnet (YIG) in 3D microwave cavities has been firstly reported in the literature [16, 17]. Likewise, USC regime to resonant cavities was also found with different magnetic materials [18–21]. In view of the realization of scalable architectures, small magnets coupled to superconducting planar resonant geometries have been recently designed and observed to achieve the (ultra) strong coupling regime [22–27]. In spite of these encouraging results, the optimization of these hybrid systems for the USC is still largely unexplored. For instance, the geometry of the hybrid superconductor-magnet system needs to be optimized in order to maximize their mutual coupling. Moreover, the superconducting materials need to be resilient to magnetic field [28], at least to extent of allowing ferromagnetic resonance (FMR) experiments, while magnetic materials may be preferably insulating in order to minimize the damping. Finally, the vicinity of a superconductor to a magnetic material may significantly affect the spectrum of excitations due to the perfect (super)conductivity and Meissner effect [25].

In this Letter, we address the problem of reaching the USC regime with planar magnetic-superconducting architectures. To this aim, we performed a series of systematic experiments designed to investigate the magnon-photon coupling with different microstrip and CoPlanar Waveguide Resonators (CPW). Transmission lines are first used to carry out broadband spectroscopy, which allows us to catalog different types of spin waves excited and to reduce the number of free parameters. The magnon-photon coupling is then studied with resonators and results compared between different geometries. For data analysis we developed a modified Hopfield model,

for which we provide exact solution. We find that the coupling of the dominant magnetic mode with photons exceeds 0.2 times the cavity frequency, thus demonstrating that USC regime is at reach with this architecture. Besides the achievement of the USC regime, we obtain that the diamagnetic term is vanishingly small.

We first present a series of transmission ( $S_{21}$ ) spectroscopy experiments carried out with linear transmission lines on the same YIG/GGG film (GGG stands for gadolinium-gallium-garnet), which has thickness  $d = 5$   $\mu\text{m}$  and lateral size of  $\approx 4 \times 3$   $\text{mm}^2$ . The external magnetic field ( $\mathbf{H}_0$ ) was applied in the plane of the film along the  $x$  direction (Fig. 1). In particular we considered three different experimental conditions: YIG film glued on a metallic microstrip line having the central conductor 500  $\mu\text{m}$  wide (case #A); YIG film glued on a superconducting YBCO CPW line having a width  $w = (17 \pm 1)$   $\mu\text{m}$  and separations  $s = (14 \pm 1)$   $\mu\text{m}$  from the lateral ground planes (case #B); YIG film pressed in contact with the same CPW line (case #C). Further details are given in [29].

Figure 2 summarizes the transmission ( $S_{21}$ ) spectra obtained by using broadband transmission lines. The  $S_{21}$ -vs- $H_0$  spectra acquired by means of the microstrip (case #A, Fig. 2(a)), show a main absorption dip in correspondence to the FMR field. The field dependence of the FMR frequency is well accounted by the Kittel relation, which, for in-plane magnetized films, reduces to [30]:

$$\omega_{FMR} = \sqrt{\omega_H(\omega_H + \omega_M)}, \quad (1)$$

where  $\omega_H/2\pi = \gamma\mu_0 H_0$  and  $\omega_M/2\pi = \gamma\mu_0 M_s$ , being  $\gamma = 28.02$  GHz/T the electron's gyromagnetic ratio,  $\mu_0 = 4\pi \times 10^{-7}$  H/m the vacuum permeability and  $\mu_0 M_s = 0.245$  T the saturation magnetization of YIG at 50 K as reported in the literature [9, 29].

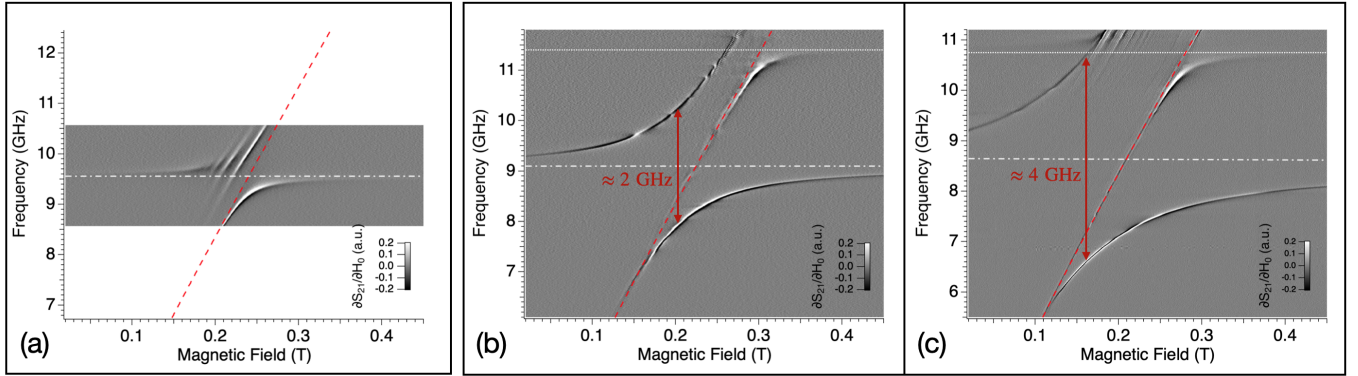


FIG. 3. Coupling of the YIG film with different planar resonators ( $P_{inc} = -8$  dBm). (a) Microstrip resonator, case #A ( $T = 50$  K). (b) CPW resonator, case #B ( $T = 30$  K). (c) YIG in contact with the CPW resonator, case #C ( $T = 30$  K). The red dashed lines show  $\omega_{FMR}(H_0)$  (Eq. 1) while the white dash-dot lines indicate the resonators' frequencies. The dotted line show the frequency of a broad box mode due to the copper cavity hosting the superconducting CPW lines.

For case #B, the numerical derivative of the transmission with respect to the magnetic field ( $\partial S_{21}(\omega, H_0)/\partial H_0$ ) is shown in Fig. 2(b). Besides the FMR mode, additional spin wave resonance (SWR) modes are well visible in this case. Such modes are commonly observed for YIG films [31, 32] and their origin is related to the profile of the microwave field  $\mathbf{h}_{ac}$ . In particular, narrow CPW lines efficiently excite travelling spin waves with finite wavevector  $0 < k \leq 2\pi/s$  [33]. Given the in-plane magnetization of the film ( $\mathbf{H}_0 \parallel x$ ) and the negligible  $x$ -component of  $\mathbf{h}_{ac}$ , we identify these excitations as Magnetostatic Surface Spin Wave (MSSW), or Damon-Eshbach modes, having dispersion law [7, 8]:

$$\omega_{MSSW} = \sqrt{(\omega_H + \omega_M)^2 - (\omega_M/2)^2} e^{-2kd}. \quad (2)$$

We can actually find a good correspondence with the measured map by assuming  $k = k_s = 2\pi/s = 4.5 \times 10^5$  rad m<sup>-1</sup> (dash-dot line in Fig. 2(b)) [34].

Figure 2(c) displays the spectrum obtained in case #C, in which the YIG film was pressed against the clean YBCO surface with no space between the two. Here the transmission spectrum shows several SWR modes whose origin can be related to the special boundary conditions imposed by the contact of the magnetic YIG with the superconducting YBCO planes, as observed in similar experiments [35, 36]. In our geometry we can assume that the Meissner effect (perfect diamagnetism) imposes the expulsion of the oscillating field at the interface. Intuitively this can be visualized as a superconducting plane reflecting the image of the magnetic excitations in YIG [37, 38]. Analysis of the portion of the spectrum can be attempted by simulations as suggested in [38], yet the dispersion law may depend on large extent on the specific materials and geometry of the problem [33]. The spectral map in Fig. 2(c) is characterized by a wide absorption band at frequency above  $\omega_{MSSW}$ , with SWR modes having typical linewidth  $10 \lesssim \kappa_m \lesssim 40$  MHz. As

expected for a YIG film in contact with a perfect conductor [39], the upper frequency limit of the absorption band extends well beyond that of Fig. 2(b) ( $k > k_s$ ) within the predicted maximum frequency  $\omega_M = \gamma\mu_0(H + M_s)$ . The appearance of additional modes at frequency below  $\omega_{FMR}$  is also predicted for films of finite size [40].

Once we have identified of the main features of the spin wave excitation spectrum, we performed experiments in a similar configuration, i.e. in place of previously reported broadband lines, with the YIG film on half-wavelength resonators having equivalent dimensions and geometries [29]. The  $S_{21}$  map taken with the microstrip resonator (case #A) is shown in (Fig. 3(a)). The lower polariton branch has an oblique asymptote with the FMR mode (Eq. 1), while the upper polariton branch is barely visible owing to multiple resonances with spin wave modes. This situation is common with other coupled YIG/resonator systems [3] and similar to the case of inhomogeneously broaden [41] or multiple [42] spin ensembles coupled to a single electromagnetic mode. From Fig. 3(a) the collective coupling strength can be roughly estimated to be of order of hundreds of MHz.

Fig. 3(b) shows the transmission map acquired by means of the YBCO CPW resonator (case #B). With respect to the microstrip, the modes of the CPW resonator are concentrated in a smaller volume giving rise to a larger spin-photon coupling ( $g_s$ ). As a result, a large anticrossing having well defined polariton branches is obtained (Fig. 3(b)). Even larger couplings were obtained when the YIG film was put in direct contact with the YBCO resonator (case #C): with this geometry the splitting raises to  $2\lambda/2\pi \approx 4$  GHz (Fig. 3(c)), a factor of  $\approx 2$  larger than case #B. Within the anticrossing gap, no additional modes are visible except for  $\omega_{FMR}$ . This suggests that the  $k = 0$  mode is weakly coupled to the CPW resonator. Additional spin wave modes are observed above  $\approx 10$  GHz due to the presence of a spurious

box mode (Fig. 3(b,c)).

We model our system by considering a quantized single-mode electromagnetic field (with  $\omega_c$  cavity frequency) interacting with an ensemble of magnetic moments. Due to the large quenching of the orbital component of  $\text{Fe}^{3+}$  in YIG, we expect a prominent Zeeman interaction of the type  $\hat{\mathcal{H}}_Z = -g_e \hat{\sigma} \cdot \mu_B \hat{\mathbf{h}}$  for a single spin. Here  $[\hat{\sigma}_j, \hat{\sigma}_k] = i\epsilon_{jkl} \hat{\sigma}_l$  are the Pauli operators,  $\hat{\mathbf{h}}$  is the magnetic field component of the cavity resonator while  $\mu_B$  is the Bohr magneton and  $g_e \approx 2$  in the case of a simple electron. However, to not exclude the possibility of having orbital angular momentum contributions in our hybrid system, we also consider this degree of freedom including a diamagnetic term, which comes from the usual minimal coupling replacement. We develop the model by considering collective operators for the spin ensemble, the quantization of both spin excitations and the electromagnetic field which allows us to introduce the respective bosonic operators  $\hat{a}$  and  $\hat{b}$ . Then, by applying the Holstein-Primakoff transformation, we obtain [29]:

$$\begin{aligned} \hat{\mathcal{H}} = & \omega_c \hat{a}^\dagger \hat{a} + \omega_b \hat{b}^\dagger \hat{b} + \lambda (\hat{b} + \hat{b}^\dagger) (\hat{a} + \hat{a}^\dagger) \\ & + \beta (\hat{a} + \hat{a}^\dagger)^2, \end{aligned} \quad (3)$$

that is the well-known Hopfield Hamiltonian [43].

We consider the dependence of the magnon resonance frequency  $\omega_b$  to the external magnetic field  $H_0$  as described by  $\omega_b = \sqrt{\omega_H(\omega_H + \omega_M)} + \Delta$ , leaving as the sole free parameter the energy shift  $\Delta$  characterizing high frequency  $k \neq 0$  magnons for the next step of our investigation. In our analysis we also leave as free parameters the cavity frequency  $\omega_c$ , the collective coupling  $\lambda$  and the factor of the diamagnetic term  $\beta$ . The eigenvalues of Eq. 3 can be derived by introducing polariton operators [29] thus obtaining:

$$\Omega_{\pm} = \frac{1}{\sqrt{2}} \sqrt{\tilde{\omega}_c^2 + \omega_b^2 \pm \sqrt{(\tilde{\omega}_c^2 - \omega_b^2)^2 + 16\omega_c\omega_b\lambda^2}}, \quad (4)$$

where  $\tilde{\omega}_c = \sqrt{\omega_c(\omega_c + 4\beta)}$ .

The above equation can fit the peaks of the  $S_{21}$  spectrum (case #C). Figure 4 shows the best fit result obtained with these parameters:  $\omega_c/2\pi = 8.65$  GHz,  $\Delta/2\pi = 2.05$  GHz, and  $\lambda/2\pi = 2.002$  GHz. For what concerns the diamagnetic parameter  $\beta$ , the only nontrivial result (i.e. nonzero result from fit) has been obtained by assuming a dependence on the magnon frequency:  $\beta = \alpha/\sqrt{\omega_b}$ , which can be justified by the fact that the presence of this term is dominant at low frequencies. With this assumption, we obtained  $\alpha/\sqrt{2\pi} = 3 \times 10^{-3}$   $\text{GHz}^{\frac{3}{2}}$ , corresponding to a value of the diamagnetic coefficient  $\beta/2\pi \sim 10^{-3}$  on resonance condition. The ratio between the collective coupling and the cavity frequency is approximately 0.23, fulfilling the criterion  $\lambda/\omega_c > 0.1$  for USC. Remarkably, the influence of the diamagnetic term

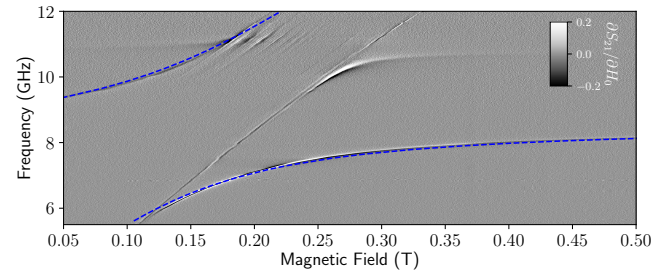


FIG. 4. Best fit of the transmission spectrum obtained in case #C with the YIG film pressed on top of the superconducting YBCO CPW. The obtained parameters are:  $\omega_c/2\pi = 8.65$  GHz,  $\Delta/2\pi = 2.05$  GHz,  $\lambda/2\pi = 2.002$  GHz,  $\alpha/\sqrt{2\pi} = 3 \times 10^{-3}$   $\text{GHz}^{\frac{3}{2}}$ . The ratio between the collective coupling  $\lambda$  and the cavity frequency is approximately 0.23, fulfilling the criterion  $\lambda/\omega_c > 1$  for USC. Moreover, the factor  $\alpha$  of the diamagnetic term is very small.

is almost negligible leading us to conclude that the system couples to the resonator mainly through the spins. Notice that its value is more than two orders of magnitude smaller than the standard diamagnetic term for electric dipolar interactions [29].

Let us check the consistency of our results. We note that the fitted value of the frequency shift  $\Delta/2\pi = 2.05$  GHz is  $\omega_{MSSW} < \Delta < \omega_M$ , thus within the band of large wavevector magnon modes observed for YIG and superconductor in direct contact (Fig. 2(c)). The spin-photon coupling depends on the mode volume of the resonator and can be evaluated as [44]

$$g_s/2\pi = \frac{1}{4} \gamma b_{vac} \quad (5)$$

with  $b_{vac} \approx \mu_0 \omega_c / (4w) \sqrt{h/Z_0}$ ,  $h = 6.626 \times 10^{-34}$  J s the Planck constant and  $Z_0 = 58 \Omega$  the nominal impedance of the CPW resonator. Since  $b_{vac} \approx 3$  nT [29], we obtain  $g_s/2\pi = 21$  Hz. For comparison, the fundamental mode of the microstrip resonator has a larger volume which results in a lower  $g_s$  (estimated to be less than 1 Hz) and in a lower collective coupling (Fig. 3(a)). Indeed, finite-element electromagnetic simulations (Fig. 1(b)) indicate that in the CPW lines  $\mathbf{h}_{ac}$  is, to a large extent, confined between the central line and the lateral ground planes in a region of approximate width  $w + 2s = 45 \mu\text{m}$  [29].

The collective coupling strength  $\lambda/2\pi = 2.002$  GHz obtained by fitting the experimental data with Eq. 4 (Fig. 4) can be spelled out as  $\lambda = g_s \sqrt{2s_{\text{Fe}} N}$ , where  $s_{\text{Fe}} = 5/2$  is the ground state spin of YIG and  $N = 1.8 \times 10^{15}$  is the total number of spins. Considering the spin density  $\rho = 2 \times 10^{28} \text{ m}^{-3}$  [3] and the effective area of  $4 \text{ mm} \times 45 \mu\text{m}$  in which the microwave field overlaps the YIG film (Fig. 1), we can estimate an upper bound  $d' \approx 0.5 \mu\text{m} \ll d$  for the thickness of the portion of YIG film coupled with the CPW resonator. This suggests that the magnon modes that are effectively coupled

to the cavity one are located in close vicinity with the superconducting resonator. This observation is supported by similar experiments we performed with 20  $\mu\text{m}$  thick YIG film, which provide results quite similar to those obtained with the 5  $\mu\text{m}$  YIG film, thus confirming that the coupling is confined within few  $\mu\text{m}$  [29]. The ratio between the collective couplings in configuration #C and #B is  $g_{s,C}/g_{s,B}\sqrt{N_C/N_B} \approx 2$  (Fig. 3(b,c)). From finite-element simulations, we estimated  $g_{s,C}/g_{s,B} \approx 2$  due to the exponential decay of  $b_{vac}$  with  $z$  distance [29]. We therefore expect  $N_C \approx N_B$ . These observations indicate that in our experiments the achievement of the USC regime takes place mainly as a consequence of the optimized magnon-photon coupling strength.

It is also worth to estimate the cooperativity that is commonly defined as  $C = 4\lambda^2/(\kappa_m\kappa_c)$  [45]. From our spectra we take  $\kappa_m/2\pi = 40$  MHz and  $\kappa_c/2\pi = 8$  MHz as decay rates of uncoupled magnon and cavity modes [29]. With these numbers, we achieve  $C = 5 \times 10^4$ . Considering the normalized parameter  $U = \sqrt{(4\lambda^2/\kappa_m\kappa_c)(\lambda/\omega_c)} = 108$ , we infer that our results ranks among the best performing physical platforms for the reaching of the USC regime [45].

The Hopfield model we used to analyze our spectra allows us to overcome the RWA approximation generally used in previous works with magnetic systems, thus providing a quantum description of the problem that can be applied to safely explore the USC regime. We stress that the analysis of the spectrum reported in the previous paragraph is quite robust since it relies on a minimal set of free parameters. Obviously, by introducing more degrees of freedom in the Hamiltonian the spectrum can also be fitted well. For instance, one may wonder whether more magnetic modes couple to cavity photons simultaneously. Results of simulations with three (and more) modes are reported in [29]. It always results that the best fit is obtained with one dominant mode, ultra-strongly coupled to the resonator's one, plus additional modes coupled more weakly. As a matter of fact, on the basis of the sole fitting of the polaritonic branches, one cannot exclude that additional magnetic excitations are involved in our and in similar experiments reported in the literature, yet the representation with only one effective mode allows putting stringent bounds to the other terms of the Hamiltonian. That is the case for the diamagnetic term, that in our analysis results vanishingly small. This result is consistent to what is expected for a pure magnetic interaction although the issue is still debated in the literature. For instance, we just mention that conclusions reported in ref. [27] lead to a finite diamagnetic contribution yet, as those authors concluded, this may arise from surface plasmonic modes or by different nature of magnetic material (permalloy). In our case, the absence of this diamagnetic term may be relevant for the observation of superradiant phase transition expected for  $\lambda/\omega_c > 0.5$ , making pure spin systems in-

teresting and unique in this perspective.

In summary, our experimental and theoretical results show the achievement of the ultra-strong coupling with a YIG film positioned in direct contact with a superconducting CPW resonator. The obtained collective coupling strength  $\lambda/2\pi = 2.002$  GHz is improved by at least one order of magnitude with respect to previous reports involving YIG films in 3D cavities [46] or bulk YIG crystals in planar resonators [22, 23]. The estimated  $\lambda/\omega_c$  ratio of 0.23 and the cooperativity  $C = 5 \times 10^4$  might be further increased by finely tuning the spin-photon coupling and decay rates along with a different choice of the fundamental mode frequency of the resonator. The very small diamagnetic coefficient (compared to standard electric dipole interactions) observed in these systems makes them suitable for exploring superradiant phase transitions [12–15].

We thank Prof. Bulat Rami for useful discussions. This work was partially supported by European Community through FET Open SUPERGALAX project (grant agreement No. 863313) and by NATO Science for Peace and Security Programme (NATO SPS Project No. G5859). MM acknowledges TUBITAK-BIDEB for the support under the 2219 scholarship program. SS acknowledges the Army Research Office (ARO) (Grant No. W911NF1910065).

---

\* mail to: [alberto.ghirri@nano.cnr.it](mailto:alberto.ghirri@nano.cnr.it)

- [1] P. Pirro, V. I. Vasyuchka, A. A. Serga, and B. Hillebrands, Advances in coherent magnonics, *Nature Reviews Materials* **6**, 1114 (2021).
- [2] Y. Li, W. Zhang, V. Tyberkevych, W.-K. Kwok, A. Hoffmann, and V. Novosad, Hybrid magnonics: Physics, circuits, and applications for coherent information processing, *Journal of Applied Physics* **128**, 130902 (2020).
- [3] B. Zare Rameshti, S. Viola Kusminskiy, J. A. Haigh, K. Usami, D. Lachance-Quirion, Y. Nakamura, C.-M. Hu, H. X. Tang, G. E. Bauer, and Y. M. Blanter, Cavity magnonics, *Physics Reports* **979**, 1 (2022).
- [4] O. O. Soykal and M. E. Flatté, Strong field interactions between a nanomagnet and a photonic cavity, *Phys. Rev. Lett.* **104**, 077202 (2010).
- [5] J. O. Artman and P. E. Tannenwald, Measurement of permeability tensor in ferrites, *Phys. Rev.* **91**, 1014 (1953).
- [6] B. A. Auld, Coupling of electromagnetic and magnetostatic modes in ferrite loaded cavity resonators, *Journal of Applied Physics* **34**, 1629 (1963).
- [7] A. P. Daniel Stancil, *Spin wave, theory and applications* (Springer New York, NY, 2009).
- [8] A. Gurevich and G. Melkov, *Magnetization Oscillations and Waves (1st ed.)* (CRC Press., 1996).
- [9] H. Maier-Flaig, S. Klingler, C. Dubs, O. Surzhenko, R. Gross, M. Weiler, H. Huebl, and S. T. B. Goennenwein, Temperature-dependent magnetic damping of yttrium iron garnet spheres, *Phys. Rev. B* **95**, 214423 (2017).

[10] A. Frisk Kockum, A. Miranowicz, S. De Liberato, S. Savasta, and F. Nori, Ultrastrong coupling between light and matter, *Nature Reviews Physics* **1**, 19 (2019).

[11] P. Forn-Díaz, L. Lamata, E. Rico, J. Kono, and E. Solano, Ultrastrong coupling regimes of light-matter interaction, *Rev. Mod. Phys.* **91**, 025005 (2019).

[12] P. Nataf and C. Ciuti, No-go theorem for superradiant quantum phase transitions in cavity qed and counterexample in circuit qed, *Nature Communications* **1**, 72 (2010).

[13] G. Mazza and A. Georges, Superradiant quantum materials, *Phys. Rev. Lett.* **122**, 017401 (2019).

[14] G. M. Andolina, F. M. D. Pellegrino, V. Giovannetti, A. H. MacDonald, and M. Polini, Theory of photon condensation in a spatially varying electromagnetic field, *Phys. Rev. B* **102**, 125137 (2020).

[15] J. Román-Roche, F. Luis, and D. Zueco, Photon condensation and enhanced magnetism in cavity qed, *Phys. Rev. Lett.* **127**, 167201 (2021).

[16] M. Goryachev, W. G. Farr, D. L. Creedon, Y. Fan, M. Kostylev, and M. E. Tobar, High-cooperativity cavity qed with magnons at microwave frequencies, *Phys. Rev. Applied* **2**, 054002 (2014).

[17] N. Kostylev, M. Goryachev, and M. E. Tobar, Superstrong coupling of a microwave cavity to yttrium iron garnet magnons, *Applied Physics Letters* **108**, 062402 (2016).

[18] G. Flower, M. Goryachev, J. Bourhill, and M. E. Tobar, Experimental implementations of cavity-magnon systems: from ultra strong coupling to applications in precision measurement, *New Journal of Physics* **21**, 095004 (2019).

[19] L. Liensberger, A. Kamra, H. Maier-Flaig, S. Geprägs, A. Erb, S. T. B. Goennenwein, R. Gross, W. Belzig, H. Huebl, and M. Weiler, Exchange-enhanced ultrastrong magnon-magnon coupling in a compensated ferrimagnet, *Phys. Rev. Lett.* **123**, 117204 (2019).

[20] M. Bialek, J. Zhang, H. Yu, and J.-P. Ansermet, Strong coupling of antiferromagnetic resonance with subterahertz cavity fields, *Phys. Rev. Applied* **15**, 044018 (2021).

[21] J. R. Everts, G. G. G. King, N. J. Lambert, S. Kocsis, S. Rogge, and J. J. Longdell, Ultrastrong coupling between a microwave resonator and antiferromagnetic resonances of rare-earth ion spins, *Phys. Rev. B* **101**, 214414 (2020).

[22] H. Huebl, C. W. Zollitsch, J. Lotze, F. Hocke, M. Greifenstein, A. Marx, R. Gross, and S. T. B. Goennenwein, High cooperativity in coupled microwave resonator ferromagnetic insulator hybrids, *Phys. Rev. Lett.* **111**, 127003 (2013).

[23] R. G. E. Morris, A. F. van Loo, S. Kosen, and A. D. Karenowska, Strong coupling of magnons in a YIG sphere to photons in a planar superconducting resonator in the quantum limit, *Scientific Reports* **7**, 11511 (2017).

[24] J. T. Hou and L. Liu, Strong coupling between microwave photons and nanomagnet magnons, *Phys. Rev. Lett.* **123**, 107702 (2019).

[25] I. A. Golovchanskiy, N. N. Abramov, V. S. Stolyarov, M. Weides, V. V. Ryazanov, A. A. Golubov, A. V. Ustinov, and M. Y. Kupriyanov, Ultrastrong photon-to-magnon coupling in multilayered heterostructures involving superconducting coherence via ferromagnetic layers, *Science Advances* **7**, eabe8638 (2021).

[26] Y. Li, V. G. Yefremenko, M. Lisovenko, C. Trevillian, T. Polakovic, T. W. Cecil, P. S. Barry, J. Pearson, R. Divan, V. Tyberkevych, C. L. Chang, U. Welp, W.-K. Kwok, and V. Novosad, Coherent coupling of two remote magnonic resonators mediated by superconducting circuits, *Phys. Rev. Lett.* **128**, 047701 (2022).

[27] I. A. Golovchanskiy, N. N. Abramov, V. S. Stolyarov, A. A. Golubov, M. Y. Kupriyanov, V. V. Ryazanov, and A. V. Ustinov, Approaching deep-strong on-chip photon-to-magnon coupling, *Phys. Rev. Applied* **16**, 034029 (2021).

[28] A. Gherri, C. Bonizzoni, D. Gerace, S. Sanna, A. Cassinese, and M. Affronte, Yba<sub>2</sub>cu<sub>3</sub>o<sub>7</sub> microwave resonators for strong collective coupling with spin ensembles, *Applied Physics Letters* **106**, 184101 (2015).

[29] Supplemental material.

[30] C. Kittel, On the theory of ferromagnetic resonance absorption, *Phys. Rev.* **73**, 155 (1948).

[31] C. Kittel, *Introduction to Solid State Physics*, 8th ed. (Wiley, 2004).

[32] Y. Kajiwara, K. Harii, S. Takahashi, J. Ohe, K. Uchida, M. Mizuguchi, H. Umezawa, H. Kawai, K. Ando, K. Takanashi, S. Maekawa, and E. Saitoh, Transmission of electrical signals by spin-wave interconversion in a magnetic insulator, *Nature* **464**, 262 (2010).

[33] I. S. Maksymov and M. Kostylev, Broadband stripline ferromagnetic resonance spectroscopy of ferromagnetic films, multilayers and nanostructures, *Physica E: Low-dimensional Systems and Nanostructures* **69**, 253 (2015).

[34] K. J. Kennewell, M. Kostylev, and R. L. Stamps, Calculation of spin wave mode response induced by a coplanar microwave line, *Journal of Applied Physics* **101**, 09D107 (2007).

[35] M. Tsutsumi, T. Fukusako, and S. Yoshida, Propagation characteristics of the magnetostatic surface wave in the ybco-yig film-layered structure, *IEEE Transactions on Microwave Theory and Techniques* **44**, 1410 (1996).

[36] D. Oates, A. Pique, K. Harshavardhan, J. Moses, F. Yang, and G. Dionne, Tunable ybco resonators on yig substrates, *IEEE Transactions on Applied Superconductivity* **7**, 2338 (1997).

[37] I. A. Golovchanskiy, N. N. Abramov, V. S. Stolyarov, V. V. Bolginov, V. V. Ryazanov, A. A. Golubov, and A. V. Ustinov, Ferromagnet/superconductor hybridization for magnonic applications, *Advanced Functional Materials* **28**, 1802375 (2018).

[38] I. A. Golovchanskiy, N. N. Abramov, V. S. Stolyarov, V. V. Ryazanov, A. A. Golubov, and A. V. Ustinov, Modified dispersion law for spin waves coupled to a superconductor, *Journal of Applied Physics* **124**, 233903 (2018).

[39] S. Seshadri, Surface magnetostatic modes of a ferrite slab, *Proceedings of the IEEE* **58**, 506 (1970).

[40] T. W. O’Keeffe and R. W. Patterson, Magnetostatic surface?wave propagation in finite samples, *Journal of Applied Physics* **49**, 4886 (1978).

[41] I. Diniz, S. Portolan, R. Ferreira, J. M. Gérard, P. Bertet, and A. Auffèves, Strongly coupling a cavity to inhomogeneous ensembles of emitters: Potential for long-lived solid-state quantum memories, *Phys. Rev. A* **84**, 063810 (2011).

[42] A. Gherri, C. Bonizzoni, F. Troiani, N. Buccheri, L. Beverina, A. Cassinese, and M. Affronte, Coherently coupling distinct spin ensembles through a high- $T_c$  superconducting resonator, *Phys. Rev. A* **93**, 063855 (2016).

- [43] J. J. Hopfield, Theory of the contribution of excitons to the complex dielectric constant of crystals, *Phys. Rev.* **112**, 1555 (1958).
- [44] G. Tosi, F. A. Mohiyaddin, H. Huebl, and A. Morello, Circuit-quantum electrodynamics with direct magnetic coupling to single-atom spin qubits in isotopically enriched  $^{28}\text{Si}$ , *AIP Advances* **4**, 087122 (2014).
- [45] P. Forn-Díaz, L. Lamata, E. Rico, J. Kono, and E. Solano, Ultrastrong coupling regimes of light-matter interaction, *Rev. Mod. Phys.* **91**, 025005 (2019).
- [46] X. Zhang, C. Zou, L. Jiang, and H. X. Tang, Superstrong coupling of thin film magnetostatic waves with microwave cavity, *Journal of Applied Physics* **119**, 023905 (2016).
- [47] C. Bonizzoni, M. Maksutoglu, A. Gherri, J. van Tol, B. Rameev, and M. Affronte, Coupling Sub-nanoliter BDPA Organic Radical Spin Ensembles with YBCO Inverse Anapole Resonators, *Applied Magnetic Resonance* (2022).
- [48] A. Gherri, C. Herrero, S. Mazerat, T. Mallah, O. Moze, and M. Affronte, Coupling nanostructured csnicr prussian blue analogue to resonant microwave fields, *Advanced Quantum Technologies* **3**, 1900101 (2020).
- [49] J. M. Sage, V. Bolkhovsky, W. D. Oliver, B. Turek, and P. B. Welander, Study of loss in superconducting coplanar waveguide resonators, *Journal of Applied Physics* **109**, 063915 (2011).
- [50] G. Eaton, S. Eaton, D. Barr, and R. Weber, *Quantitative EPR* (Springer Vienna, 2010).
- [51] D. A. Connelly, H. R. O. Aquino, M. Robbins, G. H. Bernstein, A. Orlov, W. Porod, and J. Chisum, Complex permittivity of gadolinium gallium garnet from 8.2 to 12.4 ghz, *IEEE Magnetics Letters* **12**, 1 (2021).
- [52] D. Polder, Viii. on the theory of ferromagnetic resonance, *The London, Edinburgh, and Dublin Philosophical Magazine and Journal of Science* **40**, 99 (1949).
- [53] Y. Zhang, X. S. Wang, H. Y. Yuan, S. S. Kang, H. W. Zhang, and X. R. Wang, Dynamic magnetic susceptibility and electrical detection of ferromagnetic resonance, *Journal of Physics: Condensed Matter* **29**, 095806 (2017).
- [54] A. Kreisel, F. Sauli, L. Bartosch, and P. Kopietz, Microscopic spin-wave theory for yttrium-iron garnet films, *The European Physical Journal B* **71**, 59 (2009).
- [55] A. Imamoğlu, Cavity qed based on collective magnetic dipole coupling: Spin ensembles as hybrid two-level systems, *Phys. Rev. Lett.* **102**, 083602 (2009).
- [56] T. Holstein and H. Primakoff, Field dependence of the intrinsic domain magnetization of a ferromagnet, *Phys. Rev.* **58**, 1098 (1940).
- [57] L. Garziano, A. Settineri, O. Di Stefano, S. Savasta, and F. Nori, Gauge invariance of the dicke and hopfield models, *Phys. Rev. A* **102**, 023718 (2020).

## SUPPLEMENTAL MATERIAL

### Experimental set-up

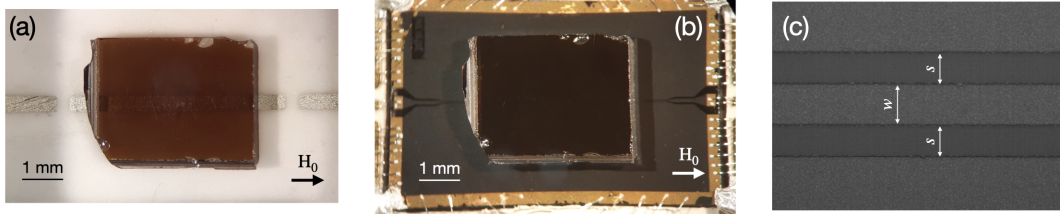


FIG. 5. Photographs of the (a) Ag/alumina microstrip resonator and (b) YBCO/sapphire CPW transmission line with the YIG/GGG film positioned on top. (c) Blow-up of the central region of the CPW line. The lateral widths are  $w = (17 \pm 1) \mu\text{m}$  and  $s = (14 \pm 1) \mu\text{m}$ .

We prepared planar resonators with different sizes and geometries, including meanders with multiple resonance frequencies and inverse anapole resonators with focused electromagnetic radiation [47], to study the coupling with different YIG samples. Here we report on two types of planar devices: microstrip and coplanar waveguide (CPW) resonator (Fig. 5). For each of them, the corresponding broadband transmission line, having the same dimensions and geometry (except for the presence of the input and output coupling gaps defining the half-wavelength resonator), has been fabricated to investigate the spin wave excitation spectrum in the different cases.

Microstrip lines were fabricated by optical lithography and wet etching of Ag films (thickness  $\approx 3 \mu\text{m}$ ), which were thermally evaporated onto alumina  $12 \times 10 \times 0.5 \text{ mm}^3$  substrates [48]. The central strip is  $500 \mu\text{m}$  wide, while two  $300 \mu\text{m}$  coupling gaps were made to define the corresponding resonator. Superconducting CPW broadband lines and resonators were fabricated from commercial  $\text{YBa}_2\text{Cu}_3\text{O}_7$  (YBCO) films (thickness  $330 \text{ nm}$ ) deposited on a sapphire substrate and diced into  $8 \times 5 \times 0.43 \text{ mm}^3$  blocks. Etching was carried out by Ar plasma in a reactive ion etching (RIE) chamber. The central conductor has typical width  $w = (17 \pm 1) \mu\text{m}$  and is separated by  $s = (14 \pm 1) \mu\text{m}$  from the lateral ground planes (Fig. 5(c)). In the CPW resonator, the coupling gaps have width  $\delta = 140 \mu\text{m}$ . The YIG sample was either glued with a layer of silicon grease having estimated thickness of  $\sim 10 \mu\text{m}$  (case #A and #B) or pressed against the YBCO surface by means of a polytetrafluoroethylene (PTFE) screw (case #C).

Reflection ( $S_{11}$ ) and transmission ( $S_{21}$ ) spectra were acquired in the 0.1-18 GHz range by means of a Vector Network Analyzer (VNA). The experiments were carried out in the 10-50 K temperature ( $T$ ) range, planar transmission lines and resonators were installed in a cryomagnetic set-up (Quantum Design PPMS) with variable temperature control and external magnetic field up to 7 T, by means of a cryogenic insert wired with a pair of silver-plated stainless steel coaxial cables connecting the low temperature stage to the external circuitry. The microstrip transmission line and resonator (Fig. 5(a)) were mounted in a brass box and connected to the coaxial line by means of two metallic pins positioned on the microstrip. Coplanar waveguide (CPW) transmission line and resonator (Fig. 5(b)) were installed in a copper box and wire bonded (Al wire) to a printed-circuit board. Gold (thickness  $200 \text{ nm}$ ) pads were patterned on the edges of the YBCO resonator to facilitate the bonding.

In all the measurements, the incident power supplied to the planar transmission line is  $P_{inc} \approx -8 \text{ dBm}$ . The number of photons can be calculated from [49]

$$n = \frac{P_{inc} Q_L 10^{-IL/20}}{\pi h f_0^2}, \quad (6)$$

where  $f_0 = \omega_0/2\pi$  is the fundamental mode frequency,  $Q_L$  is the loaded quality factor,  $IL$  is the insertion loss and  $h$  is the Planck constant. Depending on the resonator's parameters (see below), the estimated number of photons results  $n_{mic} \approx 7 \times 10^8$  for the microstrip resonator and  $n_{CPW} \approx 3 \times 10^{10}$  for the CPW resonators. In all the experiments the number of photons resulted much smaller than the estimated number of spins.

### Temperature dependence of ferromagnetic resonance spectra of the YIG film

The YIG film has been initially characterized by means of the broadband microstrip line, which allowed the acquisition of ferromagnetic resonance spectra at different excitation frequencies in the 4.5-16.5 GHz range (Fig. 6).

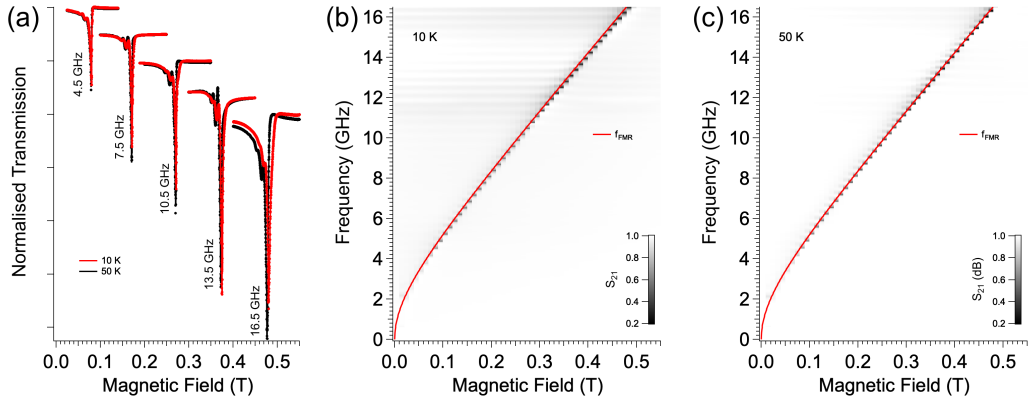


FIG. 6. Transmission spectra of the YIG film acquired by the microstrip broadband line at different temperatures. (a) Comparison between fixed-frequency field-swept spectra taken at 10 K and 50 K. (b,c) Spectral maps measured by sweeping the frequency at progressively increasing magnetic field. The temperature is (b) 10 K and (c) 50 K.

Fixed-frequency field-swept transmission spectra taken at 10 and 50 K show similar features below  $\approx 13.5$  GHz while little differences in absorption intensity and line position can be observed for higher frequencies (Fig. 6(a)). Spectra taken with the microstrip line are characterized by maximum absorption amplitude in correspondence to the FMR mode (wavevector  $k = 0$ ), while additional higher order modes have lower amplitude. The measured spectral maps (Fig. 6(b,c)) show that the dependence of the FMR mode can be fit with the Kittel formula (Eq. 1 of the Letter) by considering the saturation magnetization  $\mu_0 M_s = 0.245$  T both for 10 and 50 K.

#### Additional transmission spectroscopy data

Additional experiments have been carried out to investigate the effect of the GGG substrate (area  $\sim 4 \times 3$  mm $^2$ , thickness 0.5 mm), which is characterized by long-range ferromagnetic ordering at mK temperatures. By means of different resonators, we tested the coupling of the YIG/GGG sample at 30 K by positioning the film upside down, i.e. with the GGG substrate near the resonator and the YIG film on the opposite side. The measured transmission maps show no coupling, ruling out additional contributions from the GGG substrate. In these measurements, the presence of a faint absorption line following the Kittel relation ( $\mu_0 M_s = 0.245$  T) has been attributed to the residual absorption of the YIG film.

Fig. 7(a) shows broadband transmission-vs-frequency spectra acquired in configuration #B and #C for zero and 0.21 T applied magnetic field. In panel (b) the spectra taken at 0.21 T are directly compared to evidence the increased depth and width of the  $S_{21}$  spectrum when YIG and YBCO CPW line are put in direct contact. To quantify this point, we calculate the total absorption related to the transitions in Fig. 2(b) and (c), which can be obtained by integrating  $S_{21}(\omega)$  with respect to the frequency [50]. For  $H_0 = 0.21$  T, the ratio of the integrals calculated between 8 and 12 GHz (Fig. 7) gives  $I_C/I_B = 3.49$  [29]. The total number of magnon excitations in this frequency range thus results much larger when the YIG film is positioned in direct contact with the YBCO resonator.

Figure 8 shows  $S_{21}(\omega, H_0)$  transmission spectral maps acquired with microstrip and CPW resonators corresponding to the same dataset reported in Fig. 3 of the Letter. Since the resonator and YIG are already coupled in zero magnetic field, we exploited the resilience of YBCO resonators to high magnetic field [28] to characterize the transmission spectrum of the uncoupled CPW resonators. From transmission-vs-frequency spectra acquired at  $H_0 = 2$  T we obtain the resonator frequency  $\omega_{0,B}/2\pi = 9.1$  GHz and  $\omega_{0,C}/2\pi = 8.5$  GHz respectively for case #B and #C (Fig. 8(b) and (c)). The discrepancy between the latter and  $\omega_c/2\pi = 8.65$  GHz obtained from the fit (Fig. 4 of the Letter), indicates that at 2 T resonator and magnon modes are still weakly coupled, due to their large collective coupling strength. Since CPW resonators are fabricated from the same lithographic mask, the differences between  $\omega_{0,B}$  and  $\omega_{0,C}$  originate from specific experimental details, including sample installation in diverse ways. The insertion loss is  $IL_B = 32$  dB and  $IL_C = 30$  dB. In both cases, the loaded quality factor is  $Q_L \approx 1000$ , which is dominated by losses introduced by the GGG substrate (permittivity  $\epsilon_r = 11.99$  and  $\tan \delta = 5.2 \times 10^{-3}$  at room temperature [51]). The corresponding decay rate of the resonator ( $\kappa_0 = \omega_0/Q_L$ ) amounts to  $\kappa_{0,B}/(2\pi) = 9$  MHz and  $\kappa_{0,C}/(2\pi) = 8$  MHz. For comparison, the microstrip resonator (case #A) displays  $\omega_{0,A}/2\pi = 9.5$  GHz,  $IL_A = 42$  dB and  $Q_L \approx 120$  (Inset

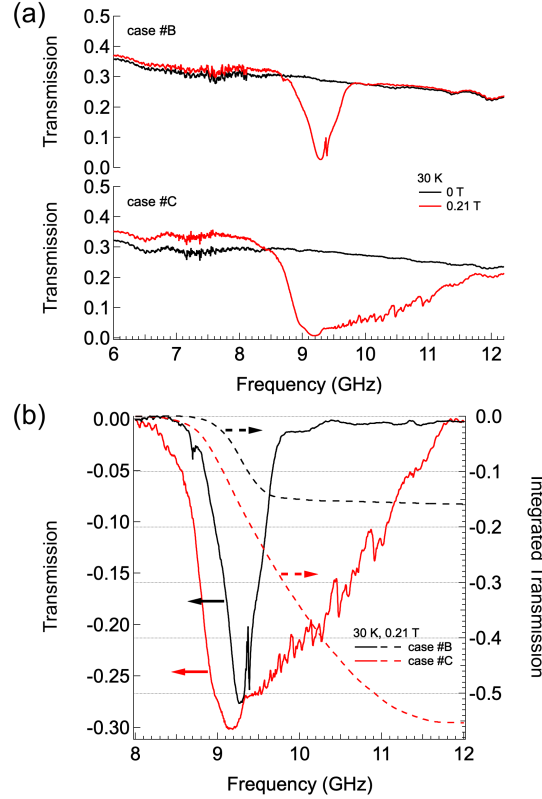


FIG. 7. Transmission spectra of the YIG film acquired by the CPW broadband line. (a) Comparison between frequency spectra taken for cases #B and #C. (b) Direct comparison between the spectra at 0.21 T after background subtraction. Dashed lines show the integral calculated between 8 and 12 GHz.

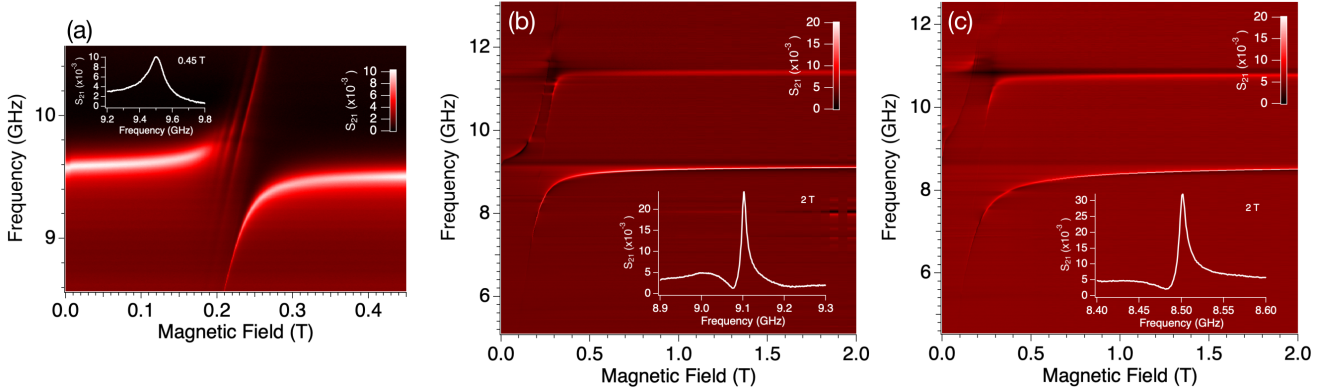


FIG. 8. Spectral maps showing the transmission of resonators coupled with the YIG film after background subtraction. (a) Metallic microstrip resonator ( $T = 50$  K, case #A). Inset: transmission-vs-frequency spectrum taken at  $H_0 = 0.45$  T. (b) Superconducting CPW resonator ( $T = 30$  K, case #B). (c) CPW resonator with the YIG film pressed against the superconductor ( $T = 30$  K, case #C). In (b) and (c) the insets show the transmission-vs-frequency spectrum taken at  $H_0 = 2$  T.

in Fig. 8(a)), resulting in the decay rate  $\kappa_{0,A}/(2\pi) = 79$  MHz.

Figure 9 shows the evolution of derivative spectra corresponding to the dataset in Fig. 3(c) of the Letter and plotted as a function of the frequency for fixed fields. The lower polaritonic branch typically shows narrower and more marked derivative peaks with respect to the upper one. This behavior is evident also in the spectra plotted in Fig. 10(a,b) as a function of the magnetic field. Transmission  $S_{21}$  and  $S_{12}$  spectra taken at positive and negative field shows a comparable behavior (panel (c)).

Figure 11 shows a direct comparison between transmission data taken with the same CPW resonator and films of

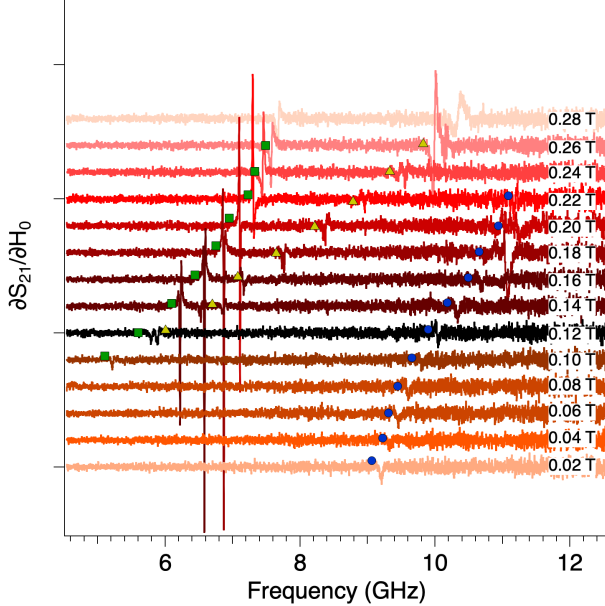


FIG. 9. Evolution of the derivative spectra (case #C) plotted as a function of frequency for fixed applied magnetic fields. Green squares and blue circles indicate respectively the position of the lower and upper polaritonic branches, yellow triangles shows the evolution of the FMR mode.

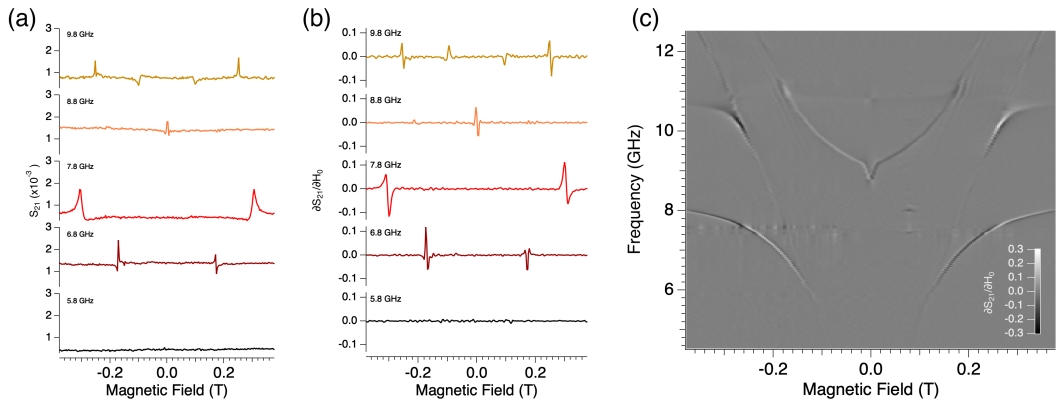


FIG. 10. Transmission spectral data taken with the YIG sample in contact with the CPW resonator.  $S_{21}$  (a) and  $\delta S_{21}/\delta H_0$  (b) spectra plotted as a function of the magnetic field for different frequencies, as indicated. (c) Spectral map acquired for  $H_0$  spanning between 0.38 to -0.38 T.

different thicknesses and sizes. In these preliminary experiments, the sample was held on the resonator with a copper spring, this resulted in a slightly lower coupling with respect to data reported in the Letter. Panel (a) shows the spectral map taken with the YIG/GGG film having a thickness of 5  $\mu\text{m}$  and an area of  $\approx 4 \times 3 \text{ mm}^2$ , as reported in the main article. Panel (b) shows data acquired on a YIG/GGG film having a thickness of 20  $\mu\text{m}$  and area of  $\approx 5 \times 1 \text{ mm}^2$ . The splitting indicated by the blue arrow, corresponding to  $2\lambda/(2\pi) \approx 3.6 \text{ GHz}$ , is consistent in both cases.

#### Finite-element electromagnetic simulations

Preliminary simulations of the electromagnetic field profile with commercial codes (CST Microwave Studio) have been used as a guide to evaluate and the distribution of the microwave field and to optimize the effective volume of interaction. The CPW resonator was modelled with realistic geometry, dimensions and materials parameters while the superconducting film was approximated as a perfect electric conductor (PEC).

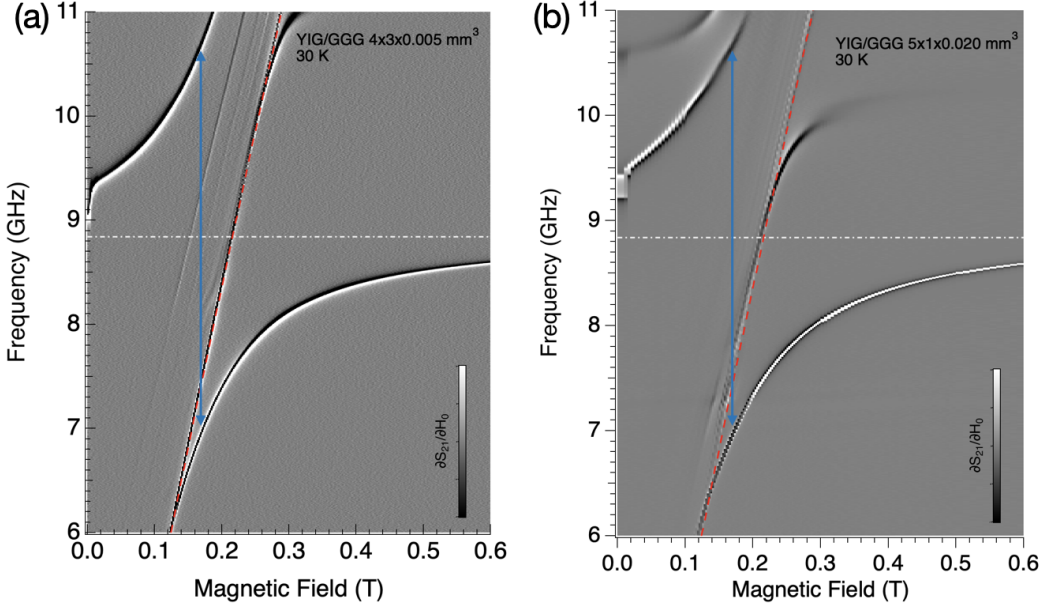


FIG. 11. Comparison between different YIG/GGG films: (a) thickness 5  $\mu\text{m}$ , (b) thickness 20  $\mu\text{m}$ . The cyan arrows indicate a splitting  $2\lambda/(2\pi) \approx 3.6$  GHz in both cases. The red dashed lines display the Kittel relation ( $\mu_0 M_s = 0.245$  T). Both measurements were carried out by means of the same YBCO CPW resonator, horizontal dash-dot lines show the frequency of the fundamental mode.

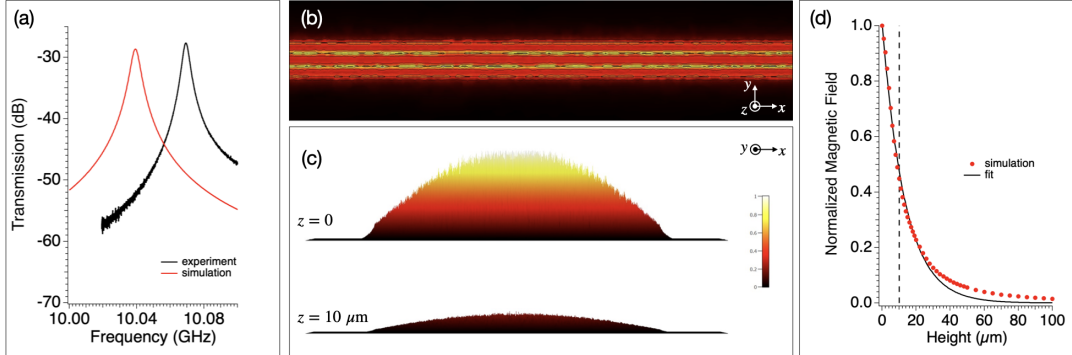


FIG. 12. Electromagnetic simulation of the bare CPW resonator. (a) Comparison between the experimental ( $T = 30$  K) and simulated spectra. (b) Spectral map showing the normalized value of  $h_{ac}$  around the central conductor. (b, c)  $x$ -dependence of the  $y$ -averaged value of  $h_{ac}$  calculated for  $z$  heights of 0 and 10  $\mu\text{m}$ . (d) Calculated dependence of the magnetic field component along the  $z$ -axis. The solid line shows the fit with Eq. 7.

We initially calculated the transmission spectrum of the bare resonator. To obtain a substantial correspondence with the measured spectrum (Fig. 12(a)), we modelled the sapphire substrate (volume  $8 \times 5 \times 0.43$   $\text{mm}^3$ ) with the permittivity  $\epsilon_r = 10.74$ , while losses were included by forcing  $\tan(\delta)$  to values higher than those expected for sapphire. The frequency of the fundamental mode results in good agreement with the value obtained from  $\omega_{c,bare}/2\pi = c/2\sqrt{\epsilon_{eff}l}$  being  $l = 6.02$  mm the length of the central strip and  $\epsilon_{eff} = 5.77$  the effective permittivity calculated for the CPW line.

The simulated distribution of the magnetic component of the fundamental mode ( $h_{ac}$ ) shows that the field is localized along  $y$  in a region of approximate width  $w + 2s = 45$   $\mu\text{m}$  around the central conductor (panel (b)). The value of  $h_{ac}$  shows a pronounced decay with increasing  $z$  distance from the upper surface of the resonator ( $z = 0$ ), as it can be seen in the profiles calculated for  $z = 0$  and 10  $\mu\text{m}$  and plotted as a function of  $x$  (Fig. 12(c)). To quantify this trend, we calculated the average of  $h_{ac}$  in regions centered in the middle of the CPW resonator (area 4 mm  $\times$  45  $\mu\text{m}$ ) with progressively increasing  $z$  height. The obtained points ( $\bar{h}_{ac}(z)$ ) show a quasi exponential

dependence from  $z$  (Fig. 12(d)) that can be fit with

$$\bar{h}_{ac}(z) = h_{max} \exp(-z/\eta) \quad (7)$$

being  $h_{max} = \bar{h}_{ac}(z = 0)$  and  $\eta = 13.5 \mu\text{m}$ . Since  $\bar{h}_{ac}(10 \mu\text{m})/h_{max} = 0.45$  and by assuming that the normalized spin-photon coupling  $g_s(z)/g_s(z = 0)$  scales as  $\bar{h}_{ac}(z)/h_{max}$ , we obtain the ratio  $g_s(z = 0)/g_s(z = 10 \mu\text{m}) = 2.2$ . This value is in good agreement with the ratio of the anticrossing splittings in configurations #C and #B derived from Fig. 3 of the Letter.

The absolute value of  $h_{max}$  obtained from the simulation can be used to estimate the amplitude of the zero-point vacuum fluctuation  $b_{vac}$ . Being  $b_{max} = \mu_0 h_{max} = 26 \text{ mT}$  the value obtained for  $P_{inc} = 0.5 \text{ W}$ , we obtain  $b_{vac} = b_{max} \sqrt{P_{vac}/P_{inc}} \approx 3 \text{ nT}$  by considering the threshold power  $P_{vac} \approx 5 \text{ fW}$  for single-photon operation (Eq. 6). On the other hand, the vacuum magnetic fluctuation can be calculated from [44]

$$b_{vac} \approx \frac{\mu_0 \omega_c}{4w} \sqrt{\frac{h}{Z_0}} \quad (8)$$

with  $h = 6.626 \times 10^{-34} \text{ J s}$  and  $Z_0 = 58 \Omega$ . From Eq. 8 we get  $b_{vac} \approx 3 \text{ nT}$  in excellent agreement with the value resulting from finite-element simulations.

As a next step we modeled the effect of a GGG substrate having volume of  $4 \times 3 \times 0.5 \text{ mm}^3$  (Fig. 12). By using  $\epsilon_r = 11.99$  and  $\tan \delta = 5.2 \times 10^{-3}$  for GGG, the simulated fundamental mode frequency  $\omega_{c,sim}/2\pi = 8.62 \text{ GHz}$  results in good agreement with  $\omega_c/2\pi = 8.65 \text{ GHz}$  obtained from the fit of the experimental data (Fig. 4 of the Letter). With respect to the bare resonator, the presence of the GGG substrate determines the shift of the fundamental mode towards lower frequency and the broadening of resonant peaks. The latter gives rise to a higher decay rate  $\kappa_c$ . As expected for CPW resonators, the simulated distribution of  $\mathbf{h}_{ac} = h_x \hat{x} + h_y \hat{y} + h_z \hat{z}$  shows an antinode in the middle of the resonator (Fig. 1 of the Letter), with the microwave field localized around the central conductor (panel (c)) and with negligible  $h_x$  as expected for a quasi-transverse electromagnetic (TEM) mode (panel (d)).

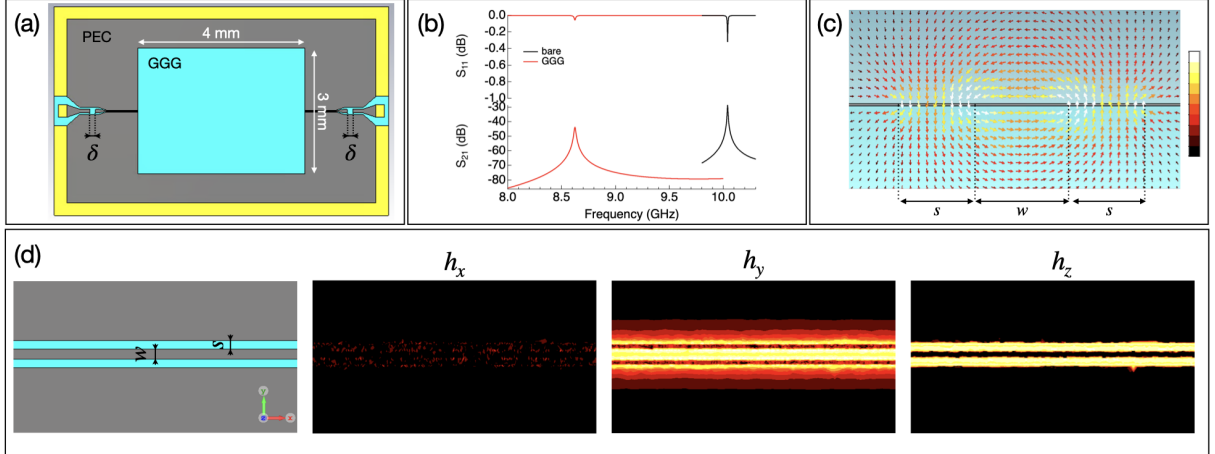


FIG. 13. Electromagnetic simulations of the CPW resonator with the GGG substrate positioned on top. (a) Representation of the model used for the simulations. Colors indicate different materials: PEC, grey; Au, yellow; GGG, cyan. (b) Simulated reflection  $S_{11}$  and transmission  $S_{21}$  spectra showing the comparison between bare resonator and GGG. (c) Vertical section of the simulated  $\mathbf{h}_{ac}$  field in the middle of the resonator (phase  $\phi = 0$ ). (d) Blow-up of the CPW line showing the simulated root-mean square cartesian components of  $\mathbf{h}_{ac}$ . Letters in (a,c,d) correspond to  $\delta = 140 \mu\text{m}$ ,  $w = 17 \mu\text{m}$  and  $s = 14 \mu\text{m}$ .

We finally carried out electromagnetic simulation to evaluate the transmission of the resonator in the presence of the YIG film, which was included to cover the lower face of the GGG substrate with a thickness  $d = 5 \mu\text{m}$ . The precession of magnetization in ferrite films can be described by the magnetic gyrotropic model, in which the permeability is assumed to be a Polder tensor with characteristic anisotropy and frequency dependence [52]. The magnetic dispersion of the YIG was defined by directly introducing the Larmor frequency  $\omega_H/2\pi = \gamma\mu_0 H_0$  and the gyrotropic frequency  $\omega_M/2\pi = \gamma\mu_0 M_s$  as input parameters of the simulator, with  $\gamma = 28.02 \text{ GHz/T}$ ,  $\mu_0 = 4\pi \times 10^{-7} \text{ H/m}$  and  $\mu_0 M_s = 0.245 \text{ T}$ .

The simulations were carried out for increasing values of the external magnetic field ( $\mathbf{H}_0 = H_0 \hat{x}$ ), the spectral maps in Fig. 14 show the evolution of the coupled YIG-resonator modes clearly displaying the appearance of polaritonic

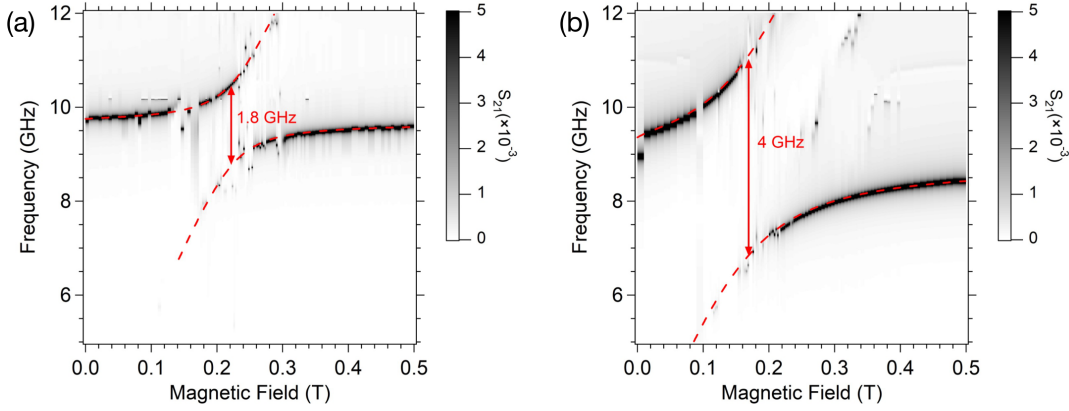


FIG. 14. Transmission spectral maps showing the evolution of coupled CPW resonator and YIG film modes obtained from finite-element electromagnetic simulations. (a) The YIG film is lifted of  $10 \mu\text{m}$  with respect to the surface of the resonator. (b) The YIG film is in contact with the resonator. Dashed lines are guides for the eye.

branches. The simulations performed with the YIG film lifted of  $10 \mu\text{m}$  (panel (a)) and in contact (panel (b)) with the CPW resonator essentially reproduce the experimental trend shown in Fig. 3 of the Letter, with a good correspondence between the estimated splittings of the polaritonic branches. This substantial agreement suggests that such large coupling strengths are consequence of the electromagnetic coupling between spin waves and microwaves. However, we have to warn that the modelization of dynamic susceptibility on the basis of the Polder tensor, as it is assumed by the simulator and commonly used to interpret ferromagnetic resonance spectra of ferrites, is strongly questioned from the theoretical point of view [53]. We have also to mention that finite element simulations fail to reproduce the polariton lineshapes shown in Fig. 9. These observations probably disclose subtle effects, whose understanding requires more sophisticated modelling of lineshapes, but this goes beyond the scope of our Letter.

### Modelling

Magnetic excitations, i.e. spin waves in magnetically ordered materials, can be described by considering the precession of the macroscopic magnetic vector  $\mathbf{M}$  around the effective local magnetic field  $\mathbf{H}_{\text{eff}}$  through the Landau-Lifshitz-Gilbert (LLG) equation, that also accounts for damping by a phenomenological term characterised by Gilbert coefficient  $\alpha$ . Exchange and dipolar interactions between different local values of  $\mathbf{M}$  can be included in the LLG equation as effective local fields,  $\mathbf{H}_{\text{exc}}$  and  $\mathbf{H}_{\text{dip}}$  respectively, that contribute to  $\mathbf{H}_{\text{eff}}$  along with the externally applied static field  $\mathbf{H}_0$ . Both exchange and dipolar interactions are naturally included in a microscopic description of a regular lattice of interacting spins [54] and relative excitations result as normal modes of the magnetically ordered systems with characteristic dispersion between energy ( $\hbar\omega$ ) and propagation wavevector ( $k$ ). For an isotropic infinite lattice, the low lying states assume parabolic dispersion law  $\omega \approx k^2$  with a characteristic stationary ( $k=0$ ) ground state (Kittel mode). Yet, for a real specimen with a specific shape, the finite size and the boundary conditions, as well as the way the antenna excites them can make the spectrum of magnetic excitations much richer with the appearance of characteristic bands.

The coupling  $\lambda$  between magnetic and microwave modes is the key parameter that needs to be compared, in the first instance, with the damping of both the magnetic system (i.e. the dissipation rate  $\kappa_m$ ) and the photon losses ( $\kappa_c$ ) of the cavity. Since  $\lambda$  determines the rate at which the two systems exchange energy and information at resonance, when  $\lambda \geq \kappa_m, \kappa_c$  we have coherent dynamics of the two systems that work in the so called *strong coupling regime*. The dipolar coupling of single spins to the oscillating magnetic component of radiation  $\mathbf{b}_{\text{vac}}$  has the relative coupling strength  $g_s/h = \frac{1}{4}\gamma b_{\text{vac}}$  which turns out to be very weak, typically of the order of 0.1 to 50 Hz for  $b_{\text{vac}} \sim \text{nT}$ . For spin ensembles, either paramagnets or magnetically ordered systems, the collective coupling strength  $\lambda = g_s\sqrt{N}$  is enhanced by a factor scaling as  $\sqrt{N}$  [55], being  $N$  the number of spins in the ensemble interacting with the electromagnetic radiation. Thus, for instance, with  $10^{12}$  to  $10^{14}$  we can get  $\lambda = g_s\sqrt{N}=1$  to 10 MHz. For a YIG sphere,  $\kappa_m$  is of the order of MHz, thus for experiments with a cavity having high quality factors, that is small  $\kappa_c$ , the strong coupling regime is achieved (see references in the main text).

The coexistence of superconductivity and magnetism is not trivial since the presence of a magnetic field can be

detrimental to the superconductor. In our experiments, the use of high critical temperature YBCO resonators, resilient to high magnetic field [28], indicates a good option for the realization of this kind of hybrid device. Our experiments also show that the contact between superconductor and magnet, and in particular the vanishing gap between the two, is critical to enhancing the coupling between magnetic and microwave modes (Fig. 3(b,c)). The direct growth of YIG on top of superconducting oxide is not trivial but there can be different options to overcome this technical issue, while the availability of commercial YIG films of excellent quality allows the easy implementation of our experiment in different geometries.

### Derivation of the Hamiltonian

We consider a quantized single-mode electromagnetic field (resonator) interacting with an ensemble of magnetic moments through the magnetic field. The total Hamiltonian then reads ( $\hbar = 1$ )

$$\hat{\mathcal{H}} = \omega_c \hat{a}^\dagger \hat{a} + \frac{\omega_b}{2} \sum_{j=1}^N \sigma_z^{(j)} + \frac{\lambda}{2\sqrt{N}} \sum_{j=1}^N \sigma_x^{(j)} (\hat{a} + \hat{a}^\dagger) + \beta (\hat{a} + \hat{a}^\dagger)^2 , \quad (9)$$

where  $\hat{a}$  ( $\hat{a}^\dagger$ ) is the photon annihilation (creation) operator,  $\omega_c$  is the cavity resonance frequency,  $\omega_b$  is the resonance frequency of a single spin,  $\lambda$  is the collective light-matter coupling, and  $\beta$  is the coefficient of the diamagnetic term.

By using the collective spin operators  $\hat{J}_z \equiv (1/2) \sum_{j=1}^N \hat{\sigma}_z^{(j)}$  and  $\hat{J}_x = \hat{J}_+ + \hat{J}_- \equiv (1/2) \sum_{j=1}^N \hat{\sigma}_x^{(j)}$ , we can apply the Holstein-Primakoff transformations [56]

$$\hat{J}_z \rightarrow \hat{b}^\dagger \hat{b} - \frac{N}{2} , \quad \hat{J}_+ \rightarrow \hat{b}^\dagger \sqrt{N - \hat{b}^\dagger \hat{b}} , \quad \hat{J}_- = \hat{J}_+^\dagger , \quad (10)$$

where  $\hat{b}$  and  $\hat{b}^\dagger$  are the magnon annihilation and creation operators respectively, which obey to the standard bosonic commutation relations. In the thermodynamic limit (i.e.  $N \rightarrow \infty$ ) we can approximate  $\hat{J}_+ \approx \sqrt{N} \hat{b}^\dagger$ .

The Hamiltonian in Eq. (3) can be expressed in terms of two non-interacting harmonic oscillators  $\hat{\mathcal{H}} = \Omega_- \hat{P}_-^\dagger \hat{P}_- + \Omega_+ \hat{P}_+^\dagger \hat{P}_+$ , where  $\hat{P}_\pm$  are the polariton operators, which are linear combinations of light and matter operators  $\hat{P}_\mu = c_1^{(\mu)} \hat{a} + c_2^{(\mu)} \hat{b} + c_3^{(\mu)} \hat{a}^\dagger + c_4^{(\mu)} \hat{b}^\dagger$ , with  $\mu = \pm$ . To fit our parameters, we need first to find the polariton frequencies, and, being a proper bosonic excitation of the system, the operator  $\hat{P}_\mu$  fulfills the equation of motion of the harmonic oscillator  $[\hat{P}_\mu, \hat{\mathcal{H}}] = \Omega_\mu \hat{P}_\mu$ . Since the polariton operator  $\hat{P}_\mu$  is a linear combination of the light and matter operators, we need to calculate first the commutator of the latter with the Hamiltonian

$$\begin{aligned} [\hat{a}, \hat{\mathcal{H}}] &= \omega_c \hat{a} + \lambda (\hat{b} + \hat{b}^\dagger) \\ [\hat{b}, \hat{\mathcal{H}}] &= \omega_b \hat{b} + \lambda (\hat{a} + \hat{a}^\dagger) \\ [\hat{a}^\dagger, \hat{\mathcal{H}}] &= -\omega_c \hat{a}^\dagger - \lambda (\hat{b} + \hat{b}^\dagger) \\ [\hat{b}^\dagger, \hat{\mathcal{H}}] &= -\omega_b \hat{b}^\dagger - \lambda (\hat{a} + \hat{a}^\dagger) , \end{aligned}$$

and the polariton frequencies  $\Omega_\mu$  are obtained by finding the positive eigenvalues of the following Hopfield matrix

$$\mathcal{M} = \begin{pmatrix} \omega_c + 2\beta & \lambda & -2\beta & -\lambda \\ \lambda & \omega_b & -\lambda & 0 \\ 2\beta & \lambda & -\omega_c - 2\beta & -\lambda \\ \lambda & 0 & -\lambda & -\omega_b \end{pmatrix} . \quad (11)$$

leading to the expression (4) given in the main text.

Despite the results shown in the main text involving one magnonic mode being quite robust, we extend the model by introducing more magnonic modes. In addition to the results shown in the main text, we present here the fit results considering three magnonic modes. The method can be straightforwardly extended from the case of single mode, and the parameters obtained from the fit are  $\omega_c = 8.64$  GHz,  $\Delta_0 = 0.23$  GHz,  $\Delta_1 = 1.92$  GHz,  $\Delta_2 = 3.17$  GHz,  $\lambda_0 = 0.192$  GHz,  $\lambda_1 = 1.93$  GHz,  $\lambda_2 = 0.2$  GHz,  $\alpha = 0.035$  GHz $^{\frac{3}{2}}$ . It is worth noting that, among the three modes, only one results to be ultrastrongly coupled with the field of the resonator, showing again how robust is to

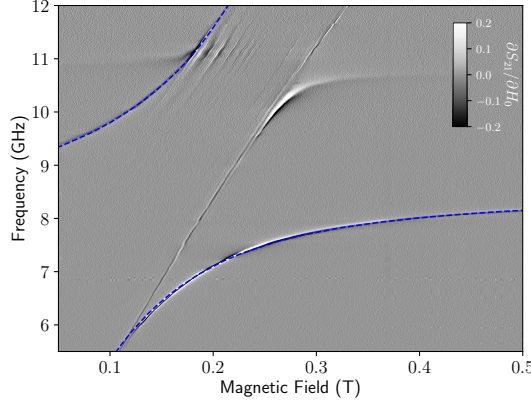


FIG. 15. Best fit of the transmission spectrum obtained in case #C with the YIG film pressed on top of the superconducting YBCO CPW. The obtained parameters, considering three magnonic modes instead of only one, are  $\omega_c = 8.64$  GHz,  $\Delta_0 = 0.23$  GHz,  $\Delta_1 = 1.92$  GHz,  $\Delta_2 = 3.17$  GHz,  $\lambda_0 = 0.192$  GHz,  $\lambda_1 = 1.93$  GHz,  $\lambda_2 = 0.2$  GHz,  $\alpha = 0.035$  GHz $^{\frac{3}{2}}$ . Among the three modes, only one is ultrastrongly coupled with the cavity field. Again, the factor  $\alpha$  of the diamagnetic term is very small.

consider only one magnonic mode. The obtained diamagnetic factor  $\alpha$  is slightly larger than the single mode case. It is useful to compare the obtained diamagnetic terms with the *standard* one  $\beta_{\text{std}} = (\lambda/\omega_c)^2 \omega_b$ , which comes from the minimal coupling replacement [12, 57] for electric dipolar interactions. Notice that the expression for  $\beta_{\text{std}}$  is fixed by gauge-invariance requirements [57]. This constraint, preventing superradiance phase transitions does not hold in the presence of magnetic interactions [12–15]. In the resonance condition ( $\omega_b = \omega_c$ ) we calculate the ratio  $\mathcal{B} \equiv \beta/\beta_{\text{std}} = \alpha\sqrt{\omega_c}/\lambda^2$ , which is  $\mathcal{B} \approx 0.002$  and  $\mathcal{B} \approx 0.027$  for the single mode and three modes cases, respectively. These results pave the way for the transition to a superradiant phase [12], as the obtained values are extremely low.